

Comparison of local structure of CrCl₃ bulk and nanocrystals above and below the structural phase transition

R. Havemann,¹ F. Hammerath,¹ P. Lepucki,¹ P. Fritsch,¹ A. P. Dioguardi ¹ M. Grönke,¹ M. Valldor ^{1,2} M. Roslova,^{1,3} A. U. B. Wolter,¹ S. Hampel,¹ T. Doert ³ H.-J. Grafe,^{1,*} S. Wurmehl,^{1,†} and B. Büchner^{1,4,5}

¹Leibniz Institute for Solid State and Materials Research Dresden, Helmholtzstr. 20, D-01069 Dresden, Germany

²Department of Chemistry, University of Oslo, NO-0315 Oslo, Norway

³Technische Universität, Faculty of Chemistry and Food Chemistry, 01062 Dresden, Germany

⁴Institute of Solid State and Materials Physics, Technische Universität Dresden, 01069 Dresden, Germany

⁵Würzburg-Dresden Cluster of Excellence ct.qmat, Germany



(Received 25 April 2023; revised 17 May 2024; accepted 3 June 2024; published 9 July 2024)

At least since the discovery of graphene and the subsequent finding of a plethora of other 2D materials, it is well anticipated that the dimensionality of a material may constitute a functional parameter. In this paper, we discuss zero-field ⁵³Cr nuclear magnetic resonance (NMR) measured in the magnetically ordered state and ³⁵Cl nuclear quadrupole resonance (NQR) data derived in the paramagnetic state of the two-dimensional van der Waals material CrCl₃, comparing the results for a bulk single crystal and a nanocrystal. In particular, we apply these spectroscopic methods to monitor the evolution of local environments in the single crystal across the structural phase transition and compare the structural and magnetic properties of a bulk single crystal and nanocrystal sample at low temperatures. The actual structural transition is reported to be of first order, where a certain hysteresis is to be expected. However, we see that both the high- and low-temperature phases coexist in both sample types across the full temperature range (300 K–1.5 K) albeit with different phase fractions. This coexistence of phases in different sample types originates in a kinetic arrest where the arrested structural domains are related to defects and stacking faults. Such defects are to a large part found in the nanocrystal but to a smaller extent in the bulk single crystal. These frozen-in phases have further consequences: The critical exponent β , derived by fitting the ⁵³Cr NMR data, is considered to denote the dimensionality of magnetic interactions. Here, the values differ considerably for both sample types. Probably, the difference in β arises from the specific domain structure of kinetically arrested phases and, in turn, from an altered interlayer magnetic exchange mediated by magnetic moments related to frozen-in domains that are related to defects and stacking faults, with their number being much higher in the nanocrystal. These findings may, in part, explain the different magnetic properties reported for different samples as their individual defect landscape determines the kinetically arrested phase fraction in CrCl₃. Hence, the structure-property relation in CrCl₃ is even more complex than anticipated.

DOI: [10.1103/PhysRevB.110.024202](https://doi.org/10.1103/PhysRevB.110.024202)

I. INTRODUCTION

The dimensionality of a material has a significant impact on its macroscopic properties. A paradigm example constitutes research on materials with two-dimensional (2D) structures, which culminated in the discovery of graphene [1,2]. Since then, a plethora of 2D materials have been identified [3], e.g., chromium(III) halides CrX₃ with X = Cl, Br, I. Chromium(III) halides form honeycomb nets of corner-sharing CrCl₆ octahedra with weak van der Waals (vdW) bonding between the 2D layers [4] and are, therefore, sometimes referred to as vdW materials [2,5]. Their specific crystal symmetry and structure is determined by the stacking sequence of the honeycomb layers [see Fig. 1(a)]. Specifically, CrCl₃ is reported to order in the monoclinic RhCl₃ structure type [space group $C2/m$; Fig. 1(b)] at ambient temperature and to undergo a crystallographic phase transition at approximately 240 K [6,7] to a rhombohedral BiI₃ structure

type [space group $R\bar{3}$; see Fig. 1(c)]. This transition relates to a change in the layer stacking arrangement with an almost unchanged intralayer structure [6,7].

The two-dimensional structure of chromium(III) halides sets the stage for their highly anisotropic magnetic properties [4,8,9] with Cr³⁺ ions as magnetic species having 3d³ electronic configuration and $S = 3/2$ spin state. Bulk samples of CrI₃ order ferromagnetically with $T_C = 61$ K [7,10,11], bulk CrBr₃ is a ferromagnet with $T_C = 37$ K [12], and bulk CrCl₃ is an antiferromagnet with an ordering temperature near 17 K [13,14]. However, the weak chemical interlayer bonding via vdW interactions favors the formation of stacking faults which in turn have consequences for the magnetic interactions [7,11] and the magnetic ordering temperature typically decreases with the increasing number of stacking faults [7]. Hence, a broad range of magnetic ordering temperatures has been reported for Cr(III) halides [6].

Upon downscaling, the magnetic properties of CrI₃, as a generic example, are determined by the number of layers, viz., by sample thickness, and change from ferromagnetic (fFM) in the bulk to antiferromagnetic (AFM) in bilayers and FM

*Contact author: h.grafe@ifw-dresden.de

†Contact author: s.wurmehl@ifw-dresden.de

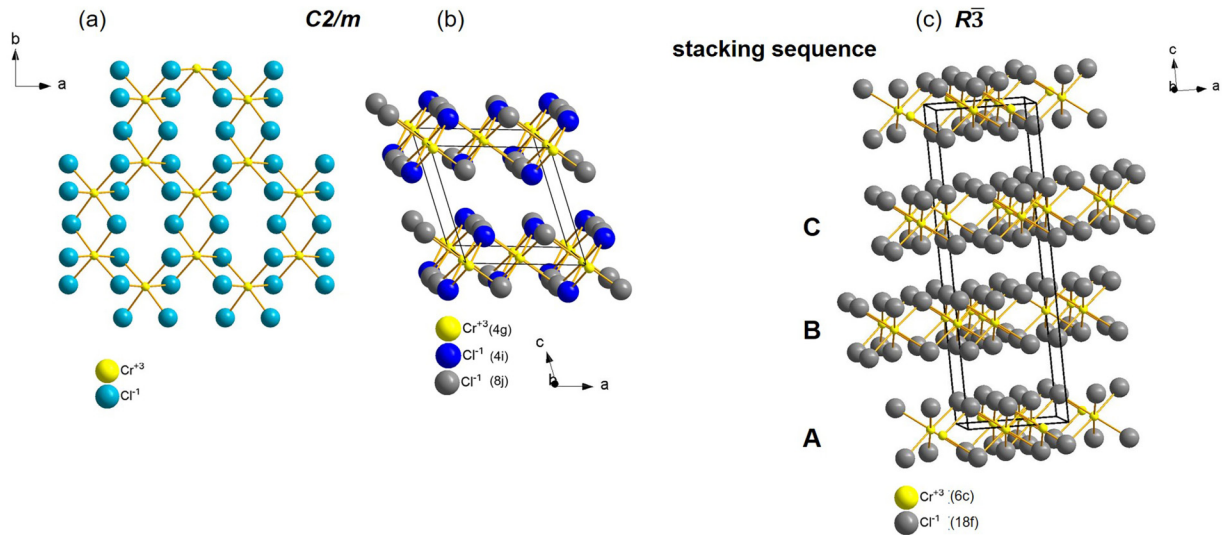


FIG. 1. (a) illustrates the honeycomb arrangement of Cr atoms in the $C2/m$ structure type in the (a, b) plane. The Cl atoms are not differentiated by their Wyckoff position. (b) shows the same structure but viewed along the monoclinic b axis where the blue Cl-1 and grey Cl-2 atoms represent the two different Cl positions and their 1:2 ratio. In this structure type, the corresponding layers have an ABABAB stacking. (c) shows the rhombohedral structure type with only one Cl position and ABCABC stacking of the layers.

in the monolayer limit [15,16]. This dependence is assumed to originate in the preferred parallel out-of-plane orientation of the magnetic moments within each layer and preferred antiparallel interlayer coupling.

The interlayer coupling is relevant for the macroscopic properties only if the number of exchange-coupled magnetic moments within a layer becomes equivalent or small compared to the number of interlayer coupled magnetic moments. As a result, a thickness-dependent crossover enables tuning of the magnetic state by choosing the number of layers.

Typically, thin layers of vdW materials are prepared by exfoliation of bulk samples and crystals where the mechanical stress originating from the exfoliation itself introduces additional stacking faults and, in turn, affects the magnetic properties. Another approach is to grow nanocrystals by short term chemical vapor transport (CVT) directly on suitable yttrium stabilized zirconia (YSZ) substrates. This has been reported to minimize the formation of stacking faults compared to the preparation by exfoliation [4].

Due to the anticipated close relationship between the stacking sequence of layers and the magnetic properties, a study of both local structure and local magnetic properties, comparing bulk and nanocrystals of chromium(III) halides, is of great interest.

In this paper, we use zero-field ^{53}Cr nuclear magnetic resonance (NMR) in the magnetically ordered state and ^{35}Cl nuclear quadrupole resonance (NQR) spectroscopy in the paramagnetic regime above and below the transition from monoclinic to rhombohedral symmetry (≈ 240 K) to probe the structural and magnetic properties comparing bulk single crystals of CrCl_3 with the corresponding CrCl_3 nanocrystals.

II. EXPERIMENTAL DETAILS

Bulk single crystals of CrCl_3 were grown by the chemical vapor transport technique starting from Cr powder (-100 mesh, 99.5%, Aldrich) and dried Cl_2 gas (99.5%, Riedel-de

Haen) according to the protocol described in Ref. [17]. The growth was carried out in a two-zone furnace. Starting materials were placed in a sealed quartz ampule which was heated up to 750°C , then the sink was slowly (1 K/min) cooled to 650°C . The obtained crystals were analyzed by SEM/EDX and x-ray diffraction, confirming the monoclinic (space group $C2/m$) room-temperature modification of the title compound [17]. Nanocrystals of CrCl_3 were derived by short-term CVT directly on suitable YSZ substrates as described in detail in Ref. [4].

Both types of samples were characterized using various techniques (see Refs. [4,17]). The magnetic properties were investigated by a superconducting quantum interference device (SQUID) magnetometer from Quantum Design (MPMS-XL). The CrCl_3 nanocrystals were measured as-grown on and with the YSZ substrate using a plastic straw where the magnetic field was applied parallel to the long axis of the substrate, hence, perpendicular to the crystallographic c axis. The magnetometry data of the same, yet uncovered YSZ substrate, were subtracted. The sample mass of the nanocrystals (mass of YSZ substrate subtracted) was 0.091 mg. The mass of the corresponding bulk single crystal was significantly larger (0.47 mg).

The NMR measurements were performed at different temperatures in an automated, coherent, phase-sensitive, and frequency-tuned spin-echo spectrometer (NMR Service, Erfurt, Germany). All bulk single crystal spectra were recorded over a frequency range 36.5 MHz–64.2 MHz with step size 0.1 MHz (exception: At 10 K, a step size of 0.05 MHz was used) with a 90° – 180° pulse of 0.8–1.6 μs pulse length with a delay between the pulses of 8 μs and a repetition time of 30 ms for $1.4 \leq T \leq 4.25$ K and 100 ms for $5 \leq T \leq 10$ K. Spectra of the nanocrystals were taken over a frequency range of 53.2–64.1 MHz with step size 0.1 MHz (4.2–8 K) and 0.5 MHz (1.5–3 K). The spectrum at 8.5 K was taken at a fixed frequency of 54.5 MHz with a 90° – 180° pulse of 0.4–0.8 μs pulse length with a repetition time of either 200 ms (1.5–3 K)

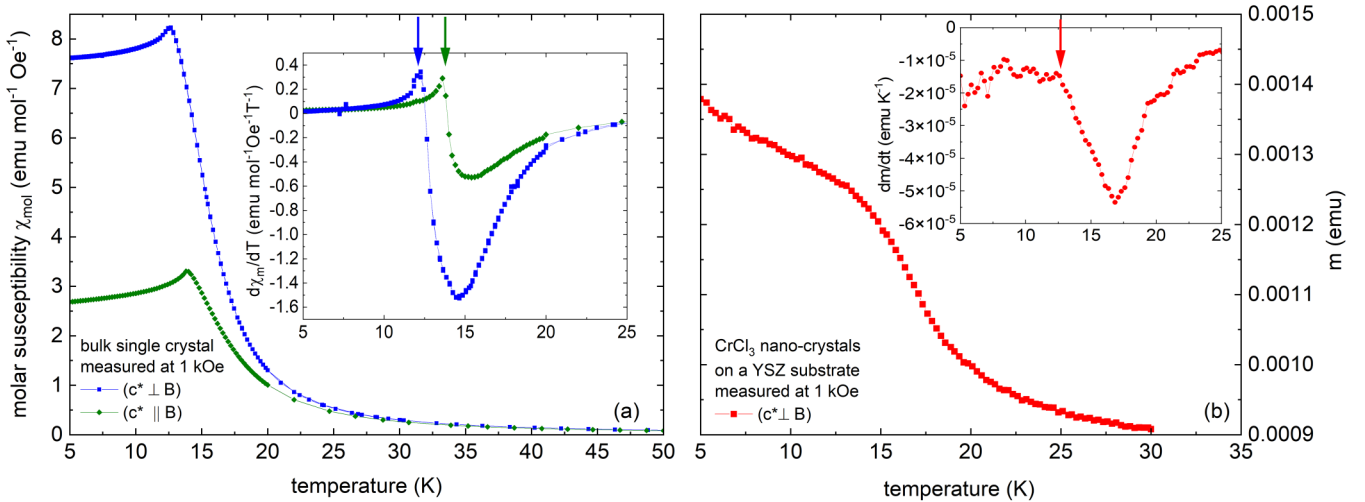


FIG. 2. Magnetization as function of temperature for (a) a CrCl₃ bulk single and (b) for CrCl₃ nanocrystals on a YSZ substrate. The bulk single crystal was measured with field parallel or perpendicular to the crystallographic c^* axis; the nanocrystals were measured perpendicular to their crystallographic c^* axis (see main text). The inset in (a) shows the first derivative of the molar susceptibility for the bulk single crystal while the inset in (b) shows the first derivative of the magnetic moment measured for CrCl₃ nanocrystal on a YSZ substrate. The susceptibility of the bare substrate (viz., before being covered with CrCl₃) was measured and this diamagnetic signal was then subtracted from the overall data (CrCl₃ on top of YSZ). However, as this approach leads to large error bars, we refrain from calculating the absolute susceptibility for the nanocrystals that is not relevant anyway for the present analysis. The Néel temperature is derived at the steepest gradient of the peak (indicated by green, blue, and red arrows, respectively).

or 50 ms (above 4.2 K). The NMR spectra were corrected for their ν^2 dependence and all spectra were normalized for their respective most prominent resonance line to allow for comparison.

The NQR measurement at room temperature was performed at a fixed frequency of 12.915 MHz. A pulse length of 5 μ s and a delay between the pulses of 18 μ s was used. The repetition time was 100 ms and the number of scans 600 000. At low temperatures, we took spectra in a frequency range from 12.915 to 13.095 MHz with a step width of 30 kHz (at 80 K), and from 12.965 to 13.095 MHz with a step width of 15 kHz (40 K). These spectra were Fourier transformed and summed up. The number of scans at low T was 60000 and the repetition time 20 ms.

The spectra were either fitted with an appropriate Gaussian model or using homemade spectral simulation software written in the Python programming language using the LMFIT package [18] to perform least-squares fitting of the ⁵³Cr zero-field nuclear magnetic resonance (ZF-NMR) spectrum. The software performs exact diagonalization of the nuclear spin Hamiltonian, allowing for an objective function to which the inputs are the characteristic NMR parameters such as the shift tensor elements K_α , the electric field gradient (EFG) tensor independent elements ν_c and η , and the internal magnetic field \mathbf{B}_{int} , etc. For this specific case the ⁵³Cr gyromagnetic ratio is taken to be $^{53}\gamma/2\pi = -2.4115$ MHz/T and the nuclear quadrupole moment $Q = -0.15 \times 10^{-28}$ m² [19].

The center of gravity of the zero-field NMR spectrum was determined by the method of moments [20], using a Simpson integration method SCIPY.INTEGRATE.SIMPSON in Python. The center of gravity is given by the first moment,

$$M_1 = \frac{1}{M_0} \int_{f_{\text{min}}}^{f_{\text{max}}} f S(f) df, \quad (1)$$

where $M_0 = \int_{f_{\text{min}}}^{f_{\text{max}}} S(f) df$ is the zeroth moment, $S(f)$ is the spectral function that describes our NMR spectrum, and f_{min} and f_{max} are the frequency limits of integration.

We then use the second moment,

$$M_2 = \frac{1}{M_0} \int_{f_{\text{min}}}^{f_{\text{max}}} (f - M_1)^2 S(f) df, \quad (2)$$

to determine the variance of the spectrum, followed by determining the standard deviation, shown as error bars in Fig. 6. Note that we chose the integration limits such that the full observable spectrum was contained for the nanocrystal, but for the single crystal we excluded the low-intensity peaks at higher frequencies. This method allowed us to extract the uncertainty of the center of gravity in a quantitative way despite the fact that the spectra are not all described by the same number of peaks over the measured temperature range.

III. RESULTS AND DISCUSSION

A. Magnetic properties of CrCl₃ as bulk single and as nanocrystal

Figure 2 shows (a) the molar susceptibility of a CrCl₃ bulk single crystal and (b) the magnetic moment of CrCl₃ nanocrystals measured on a YSZ substrate as function of temperature. The inset in (a) shows the first derivative of the molar susceptibility for the bulk single crystal while the inset in (b) shows the derivative of the magnetic moment. The Néel temperature is derived at the steepest gradient of the peak [indicated by green, blue, and red arrows in Figs. 2(a) and 2(b)], revealing T_N to be approximately 13 ± 1 K for both sample types in rough agreement with previous magnetization studies on this material, although lower than reported for highly ordered crystals [13,14,21,22]. Please note that the

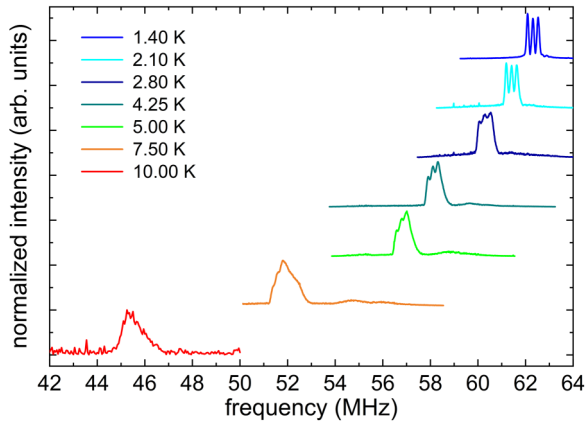


FIG. 3. Zero-field ^{53}Cr NMR spectra of a CrCl_3 bulk single crystal recorded between $1.4 \text{ K} \leq T \leq 10 \text{ K}$.

small difference in the transition temperature for H parallel and perpendicular to the c axis of the CrCl_3 bulk single crystal originates in an anisotropic magnetic exchange within and perpendicular to the vdW layers and has been previously reported, e.g., for RuCl_3 [23,24].

B. CrCl_3 studied by ^{53}Cr nuclear magnetic resonance spectroscopy in the magnetically ordered state

Figure 3 shows the zero-field ^{53}Cr NMR frequency spectra of a CrCl_3 single crystal at various temperatures between $1.4 \text{ K} \leq T \leq 10 \text{ K}$ in the magnetically ordered state. The spectra taken at low temperatures $1.4 \text{ K} \leq T \leq 5 \text{ K}$ consist of a clearly discernible three-peak-spectrum. This quadrupole-split spectrum shifts to lower frequencies with increasing temperature and seems to merge at higher temperature as those spectra taken above 5 K consist of only one broad resonance line.

Figure 4 shows the corresponding zero-field ^{53}Cr NMR frequency spectra of a CrCl_3 nanocrystal at various temperatures between $1.5 \text{ K} \leq T \leq 8.5 \text{ K}$. All spectra of the nano-crystal seem to consist of two sets of similar spectral features as seen in the bulk data, namely, two three-peak-spectra at low temperature and two broader lines at higher temperatures.

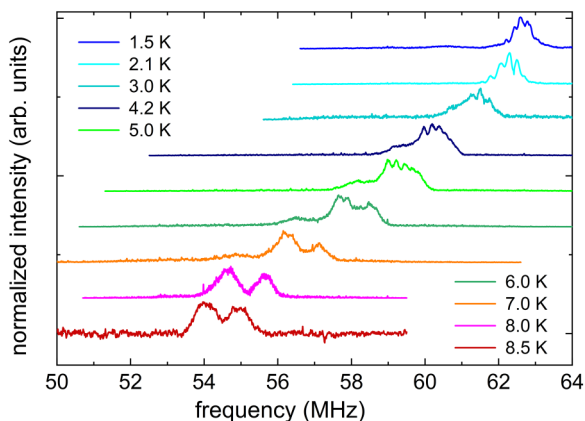


FIG. 4. Zero-field ^{53}Cr NMR spectra of a CrCl_3 nano crystal recorded between $1.5 \text{ K} \leq T \leq 8.5 \text{ K}$.

We illustrate the differences between the spectra of the bulk single crystal and the nano-crystal and, in particular, the doubling of the spectral features for the latter in more detail. For that, we plot the data taken at representative low- [2.1 K; Fig. 5(a)] and high-temperature [Fig. 5(b)] regimes. The spectra for the high-temperature regime were taken at 8.0 K for the nanocrystal (magenta dots) and at 7.5 K for the bulk single crystal (orange dots), respectively.

At the lowest temperature, we see a quadrupole-split spectrum for the bulk single crystal and at least two three-peak-spectra for the nanocrystal. A fit of the single crystal data taken at 1.4 K with Gaussian lines reveals the three lines at 62.09 MHz, 62.31 MHz, and 62.53 MHz (spacing approximately 0.22 MHz). Their full-width-half-maximum (FWHM) is comparable (0.12 MHz) as well as their spectral weight. The resonances of the nano-crystal show an unsystematic and broader distribution of both spacing and FWHM along with variable spectral weight. Hence, even two quadrupole-split sets of resonances may not be sufficient to explain all spectral features seen for the nanocrystal. The best congruence with respect to FWHM and spacing between the bulk single crystal and the nanocrystal spectrum is achieved upon shifting the latter by -0.873 MHz . In this case, the three highest intensity lines of the nanocrystal spectrum match the quadrupole-split bulk single crystal spectrum [see inset of Fig. 5(a)], but with two additional lines on the low- and one on the high-frequency site.

The bulk crystal spectrum at $T = 7.5 \text{ K}$ [orange data set in Fig. 5(b)] is approximated by a broad resonance line at 51.94 MHz [Fig. 5(a)], FWHM is $\approx 0.99 \text{ MHz}$. The nanocrystal spectrum taken at 8 K shows two broad lines at 54.61 MHz (FWHM about 0.74 MHz) and at 55.66 MHz (FWHM $\approx 0.51 \text{ MHz}$). The ratio of their spectral weight is roughly 66:36. The spacing between the two lines of the doublet is rather small and about 1.04 MHz. Interestingly, the spectrum of the bulk single crystal shows two additional small resonances that nicely match in terms of line width and frequency with the main broad double feature seen in the spectrum for the nanocrystal at high temperature. This indicates that the environment that constitutes the dominant component in the nanocrystal at 8 K is also found in the bulk sample but to a smaller extent.

We further analyze the differences at temperatures $1.4 \text{ K} \leq T \leq 10 \text{ K}$ for both sample types by comparing the evolution of the corresponding center of gravity of each zero-field NMR spectrum (see Sec. II for details), which is a measure of the average internal field.

We performed a fit with

$$f_{\text{int}} = f_{\text{int},0} \left(1 - \frac{T}{T_N}\right)^\beta \quad (3)$$

to each data set, individually yielding the Néel temperature, the critical exponent β , and the saturation value of the frequency at zero temperature $f_{\text{int},0}$. The data were weighted by the uncertainties in the least-squares fitting. The best fit and corresponding parameters are shown in Fig. 6.

At high temperature, there is a significant gap between the internal fields of the nanocrystal and the bulk single crystal; the magnitude of this gap is not constant but decreases with decreasing temperature and finally converges at zero

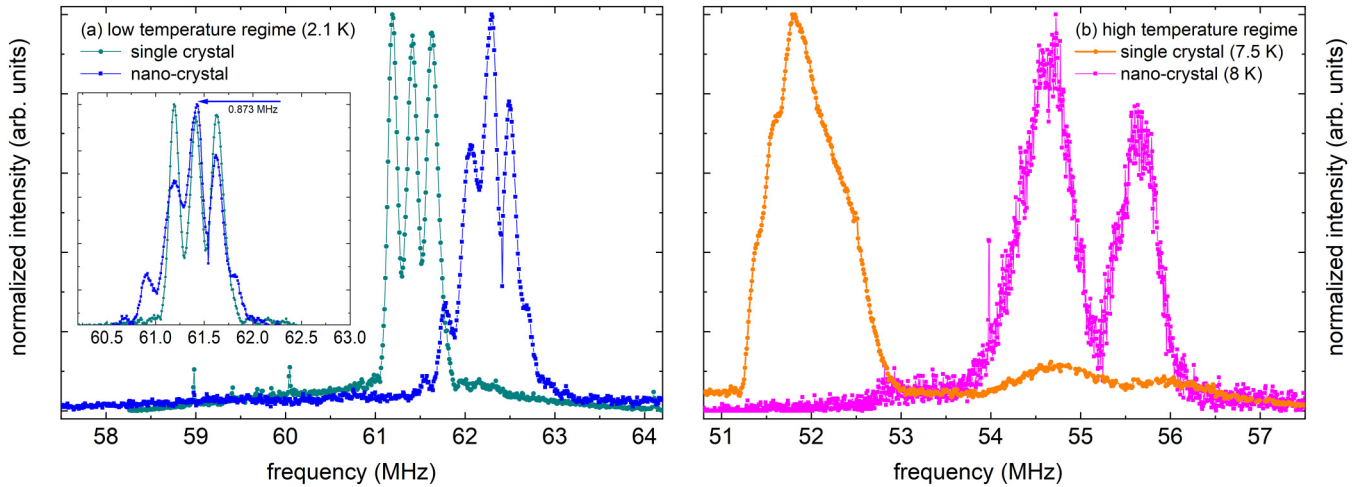


FIG. 5. (a) Zero-field ^{53}Cr NMR spectra measured at 2.1 K (low temperature regime) for the bulk single crystal (teal dots) and for the nanocrystal (blue dots). (b) Zero-field ^{53}Cr NMR spectra for the high temperature regime, measured at 8.0 K for the nanocrystal (magenta dots) and at 7.5 K for the bulk single crystal (orange dots), respectively. The inset of (a) shows the data taken at 2.1 K with the spectrum of the nanocrystal shifted by 0.873 MHz as one variant of line matching (see text).

temperature. The resulting saturation value of the frequency at zero temperature $f_{\text{int},0}$ is 64.2 ± 0.1 MHz for the bulk single crystal and 64.0 ± 0.1 MHz for the nanocrystal, indicative of comparable average internal fields at zero temperature. The Néel temperature is $T_{N,\text{sx}} = 13.7 \pm 0.3$ K for the bulk single crystal and $T_{N,\text{nx}} = 13.4 \pm 0.5$ K consistent with the magnetic data (compare Sec. III A).

The critical exponent β is, in general, considered a criterion for the dimensionality of magnetic interactions. In the present case, the fit yields $\beta = 0.27 \pm 0.01$ for the bulk single crystal and 0.16 ± 0.01 for the nanocrystal. The value derived for the bulk single crystal is in pretty good agreement with those previously reported for quasi-2D systems with XY or anisotropic Heisenberg type interactions [25,26]. The value of the critical exponent for the nanocrystal is close to that for a system with Ising spins on a two-dimensional crystal lattice,

where the critical exponent β for $T < T_N$ is reported to be about 0.125 [27,28].

Considering the NMR spectra of the two samples, the origin of their different exchange interaction may be related to their individual defect landscape as the bulk single crystal shows rather sharp lines, indicative of a small number of defects and stacking faults, while the two sets of spectral features seen for the nanocrystal hint at a much larger number of defects therein. In a recent work, Qian *et al.* [29] identified the magnetic moments of antisite Mn atoms in $\text{Mn}(\text{Bi}_{1-x}\text{Sb}_x)_4\text{Te}_7$ as mediators for interlayer ferromagnetic coupling that competes with the antiferromagnetic superexchange coupling. The defects in the nano-crystal, similarly to the Mn antisites in $\text{Mn}(\text{Bi}_{1-x}\text{Sb}_x)_4\text{Te}_7$, may alter the interlayer magnetic exchange paths thereby altering the critical exponent β .

These observations are consistent with our magnetometry data where the magnetic transition temperature of both samples is comparable, albeit rather sharp for the bulk crystal and smeared out for the nanocrystal.

C. Rationalizing the structure environments of ^{53}Cr and ^{35}Cl

CrCl_3 orders in a monoclinic RhCl_3 -type structure (space group $C2/m$) at temperatures above 240 K [6] (compare Fig. 1), yielding two crystallographic Cl positions (Wyckoff positions $4i$ and $8j$) with a multiplicity ratio as given by the Wyckoff indices of 1:2. Cl-1 ($4i$) has two Cr first-nearest neighbors at about 2.347 Å distance, while Cl-2 ($8j$) has one Cr nearest neighbor at 2.340 Å distance and the second nearest at 2.342 Å distance. Cr is surrounded by two Cl-2 atoms at 2.340 Å and two Cl-2 atoms which are only marginally more distant (2.342 Å). Cr has also two Cl-1 neighbors at 2.347 Å.

In the rhombohedral structure, viz., below 240 K, there is one position for Cr (Wyckoff position $6c$) and one position for Cl (Wyckoff position $18f$), consistent with one unique crystallographic environment for each nucleus (compare Fig. 1) and a 1:3 multiplicity. Consequently, Cr is octahedrally coordinated by six Cl atoms in the first shell; the layer stacking

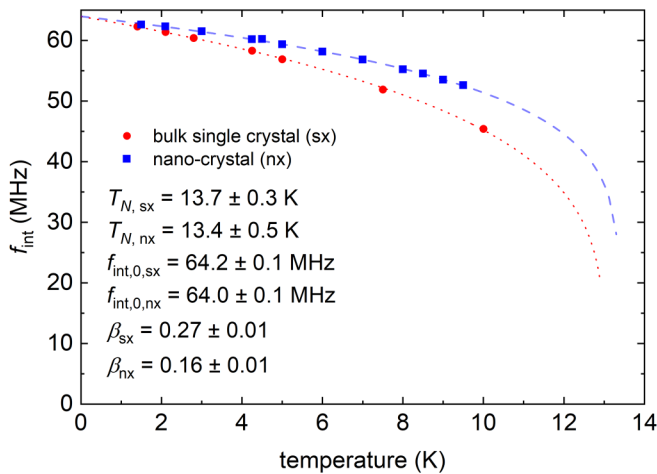


FIG. 6. Center of gravity of the zero-field ^{53}Cr NMR spectra as a function of temperature for a CrCl_3 bulk single crystal (sx: red markers) and a CrCl_3 nanocrystal (nx: blue markers) and the corresponding fits to the data (see text for details).

sequence is ABCABC (compare Fig. 1) and, hence, the EFG tensor is of high symmetry, i.e., $\eta = 0$.

Therefore, the ^{35}Cl NQR spectroscopy is expected to show two distinct lines at ambient temperature and one distinct line at 5 K due to the first-order structural phase transformation, consistent with the transformation from the two Cl positions in the monoclinic structure that merge to one only one local environment upon approaching the structural transition temperature.

D. Simulation of the low-temperature ^{53}Cr NMR spectrum

Towards a more quantitative analysis, we simulated the ^{53}Cr zero-field nuclear magnetic resonance (ZF-NMR) spectrum of the bulk single crystal measured at 1.4 K using a home-made spectral simulation software performing least-squares fitting. Nuclei with spin $I > 1/2$ in an anisotropic charge environment have a finite electric quadrupole moment eQ with e the elementary charge and Q the nuclear quadrupole moment. In the presence of an EFG at the atomic site, the nuclear electric quadrupole energy levels are not degenerate anymore. This is described by the following Hamiltonian:

$$H = \frac{3eQV_{zz}}{4I(2I-1)} [3I_z^2 - I(I-1) + \frac{\eta}{2}(I_+^2 + I_-^2)]. \quad (4)$$

The corresponding coordinate axes are defined by the principal axes of the EFG tensor. By exact diagonalization of the nuclear spin Hamiltonian (equation 4), we yield characteristic NMR parameters such as the shift tensor elements K_α , the EFG tensor with the corresponding tensor components $V_{ij} = \delta^2 V / \delta x_i \delta x_j$, the principal component of the EFG tensor along c direction (ν_c), the asymmetry of the EFG tensor ($\eta = (V_{xx} - V_{yy})/V_{zz}$), the nuclear quadrupole moment (Q), and the internal magnetic field \mathbf{B}_{int} .

The nuclear quadrupolar moments interact with the EFG tensor, yielding a resonance at the frequency

$$\nu_Q = \frac{3eQV_{zz}}{2I(2I-1)h} \sqrt{1 + \frac{\eta^2}{3}}, \quad (5)$$

where h is the Planck's constant.

To decide on the orientation of the EFG tensor with respect to the internal field at the Cr site in CrCl_3 , we followed the analysis of Narath and Fromhold [30–32] and Cable *et al.* [14]. In an earlier work, Narath [32] found that the central component of the spectrum of CrCl_3 is shifted by a second-order effect to slightly higher frequency (-6 kc/sec) relative to the satellites, which suggests the EFG is along the c axis. In 1963, Narath [30] concluded that the hyperfine field at the Cr nucleus in CrCl_3 is negative with respect to the direction of the magnetization. Hence, the internal field \mathbf{B}_{int} is perpendicular to the c axis and to the EFG, viz., aligned along the crystallographic a axis, therefore the internal field being in the vdW layers. The Cr atoms are octahedrally coordinated by six Cl atoms (compare Fig. 1 and Sec. III C). On that account, the EFG tensor is of high symmetry, i.e., $\eta = 0$.

We start with the least-squares spectral fitting of the single-crystal spectrum (blue dots in Fig. 7). The best fit is given by the red curve in the same figure. The parameters that characterize this best fit are summarized in Table I.

Based on the simplest structural model [6], we assume only one ^{53}Cr crystallographic position at 1.4 K (see Sec. III C)

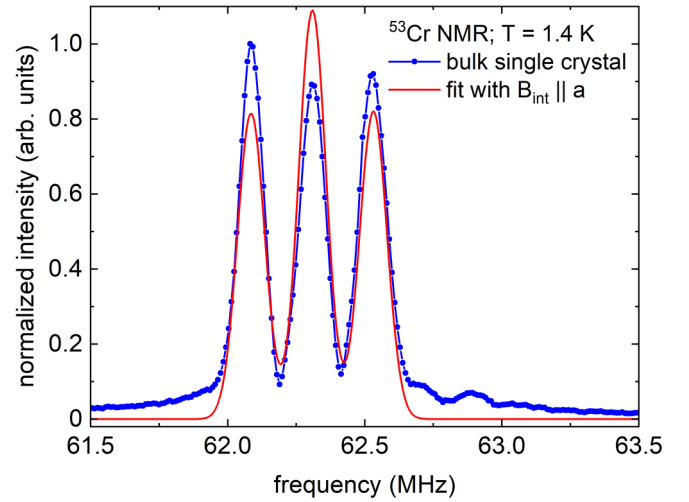


FIG. 7. Normalized intensity of the zero-field ^{53}Cr NMR response as a function of frequency for a bulk single crystal of CrCl_3 at $T = 1.4$ K [same data as in Figs. 3 and 5(b)]. The red curve is the best fit to the data with assuming the internal field \mathbf{B}_{int} is fixed along the crystallographic a axis, corresponding to the internal field being in the vdW layers, following Narath and Fromhold [30,31] and Cable *et al.* [14].

and vary four of the above variables during fitting, namely: (i) The amplitude controlling the overall spectral weight being a multiplicative factor that allows the simulation to be scaled to match the experimental spectrum. (ii) The FWHM. Incidentally, if we let FWHM vary, this would allow for different linewidths of the satellite resonances (due to a distribution of EFG parameters) with respect to the magnetic spectral broadening that affects all resonances equally (due to, in this case, a distribution of internal hyperfine fields in the magnetic state). (iii) The hyperfine field in the a direction H_{int}^a , that is, the hyperfine field component perpendicular to the principal component of the EFG tensor and ν_c the principal component of the EFG tensor. We find $H_{\text{int}}^a = 25.84$ T and $\nu_c = 0.446$ MHz. In summary, the simulation describes our data rather well (Fig. 6).

We refrain from fitting on the multisite spectrum observed in the nanocrystal. As discussed above, this spectrum appears to have at least three additional peaks, which indicates the existence of at least one different local magnetic or charge environment. Further measurements and simulations may be helpful to constrain the parameter space and allow curve fitting to aid in understanding the spectrum.

E. ^{35}Cl nuclear quadrupole resonance spectroscopy above and below the structural transition temperature

At this point, we need to remind ourselves that the early work by Narath reports on the evolution of several resonance lines that dominate the NQR spectrum at a specific temperature range that are not necessarily linked to structure or transition temperatures seen by x-ray diffraction [6]. Also, McGuire *et al.* reported a rather broad first-order phase transition [7,22,33].

As the NQR signal intensity is weaker at high temperatures, we measured a conglomerate of several bulk single

TABLE I. The parameters that characterize the best fit.

Fit Statistics	
Fitting method	least squares
Function evals	47
Data points	632
Variables	4
χ^2	1.08
Reduced χ^2	0.002
Akaike information criterion	-4018.74
Bayesian information criterion	-4001.94
Variables	
H_0 [T]	0 (fixed)
Offset	0 (fixed)
Amplitude ⁵³ Cr	0.0135 ± 0.001 (1.00%) (init = 0.05)
K_a ⁵³ Cr	0 (fixed)
K_b ⁵³ Cr	0 (fixed)
K_c ⁵³ Cr	0 (fixed)
ν_a ⁵³ Cr [MHz]	-inf (fixed)
ν_b ⁵³ Cr [MHz]	-inf (fixed)
ν_c ⁵³ Cr [MHz]	0.446 ± 0.002 (0.38%) (init = 0.5)
η ⁵³ Cr	0 (fixed)
H_a^{int} ⁵³ Cr [T]	$25.84 \pm 2.63 \times 10^{-04}$ (0.00%) (init = 25.83)
H_b^{int} ⁵³ Cr [T]	0 (fixed)
H_c^{int} ⁵³ Cr [T]	0 (fixed)
ϕ_z (deg) ⁵³ Cr [degree]	0 (fixed)
θ_{xp} (deg) ⁵³ Cr [degree]	0 (fixed)
ψ_{zp} (deg) ⁵³ Cr [degree]	0 (fixed)
FWHM ⁵³ Cr [MHz]	0.116 ± 0.001 (1.09%) (init = 0.1)
FWHM ν_Q ⁵³ Cr [MHz]	0 (fixed)
Correlations (unreported correlations are < 0.100)	
C (amplitude ⁵³ Cr, FWHM ⁵³ Cr [MHz])	0.500

crystals to yield the temperature-dependent NQR data. The expected changes in the ³⁵Cl NQR spectra (see Sec. III C for details) were monitored at ambient temperature, at 80 K and at 40 K as well as at 70 K, 60 K, and at 50 K (with similar conclusions, data not shown). Using the same setup, the same coil, and similar parameters did not enable us to measure NQR data for the nanocrystal at 295 K even though data accumulation lasted for five days.

The ambient temperature ³⁵Cl NQR spectrum of the CrCl₃ bulk single crystal [Fig. 8(a)] shows two distinct peaks that seem to reside on top of a rather broad line. The two pronounced and sharp resonances are consistent with the two Cl positions of the monoclinic structure type and their 1:2 multiplicity ratio. At 80 K, well below the anticipated structural transition temperature, the NQR spectrum consists of mainly one rather sharp resonance line. Besides the expected small shift to higher frequencies, the spectra obtained at 40 and 80 K are very similar.

Not all spectral weight in the ambient temperature spectrum is covered by the monoclinic structure. As the simplest approach, we assumed disorder in higher coordination shells where both types of Cl sense the differing environments individually, however, four Gaussian lines do not account for the full spectrum at ambient temperature, but Voigt-type lines do (not shown). The Voigt-type function is mathematically a convolution of a Lorentz and a Gaussian profile and is used to describe a line broadening by two contributions.

As a next-fit model, we assigned the spectral weight not covered by two sharp Gaussian lines to a broad distribution of slightly different environments of the two Cl nuclei (e.g., in higher coordination shells), leading to a broad continuum of overlapping resonances.

A fit based on this model to the high temperature ³⁵Cl data with two sharp and one broad Gaussian line yields the maxima of the two sharp lines at 12.90 MHz and 12.94 MHz. Their ratio is about 1:2.1, which roughly matches with the expected

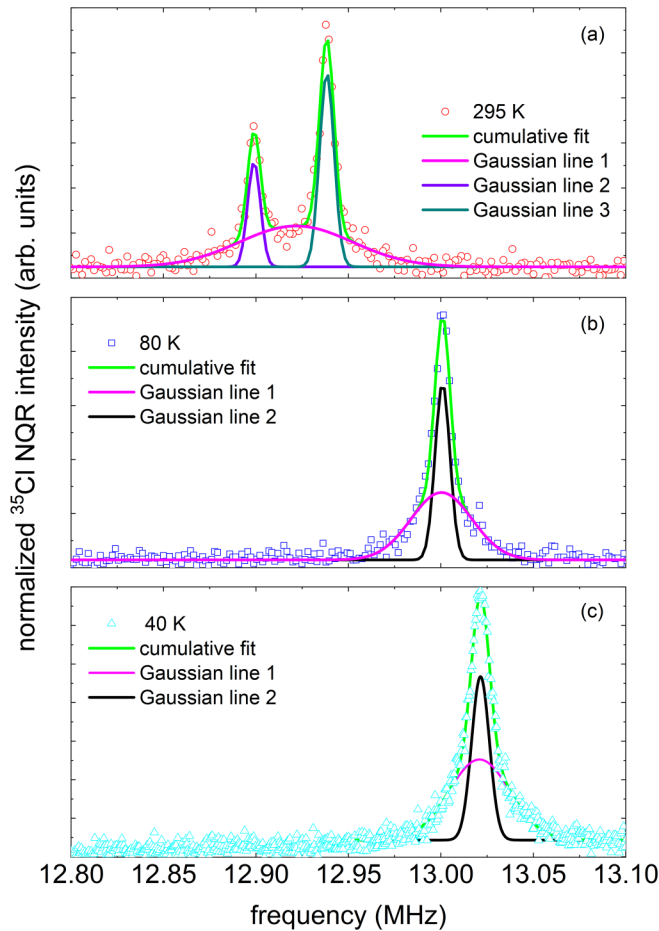


FIG. 8. (a) ^{35}Cl NQR data of the CrCl_3 bulk single crystal measured at (a) ambient temperature, (b) at 80 K, and (c) at 40 K.

multiplicity ratio. The center of gravity of the broad resonance line is right between the sharp resonance at about 12.92 MHz, corresponding to its right in the middle between the sharp lines. The sharp lines have a comparable FWHM of ≈ 9 kHz while the broad Gaussian line has a FWHM of 72 kHz. The spectral ratio of all three resonances is about 1:2.1:3.5.

At 80 K, the spectrum can be roughly approximated by a fit with two Gaussian lines at 13.00 MHz. The sharp resonance line has a FWHM of about 9 kHz, while the FWHM of the broad Gaussian lines is 34 kHz. Their spectral weight is 6.9:7.8. The center of the two lines at 40 K are at the same frequency (13.02 MHz) but also with very different FWHM of 11 kHz (sharp line) and 39 kHz; their spectral ratio is roughly 5:9.

To illustrate the changes in the spectra, we plot the NQR data taken at different temperatures (Fig. 9) shifted by hand to match on top of each other. We clearly see that the data at 80 K and at 40 K resemble each other while the line width of the 80 K line is slightly smaller than the one at 40 K. A broad contribution is found in all spectra and the evolution of spectral weight at both sides of the main lines is consistent in all data sets. However, although adding the broad line to match the spectra is a good approximation to the data, one additional broad line representing different Cl environments may be oversimplified.

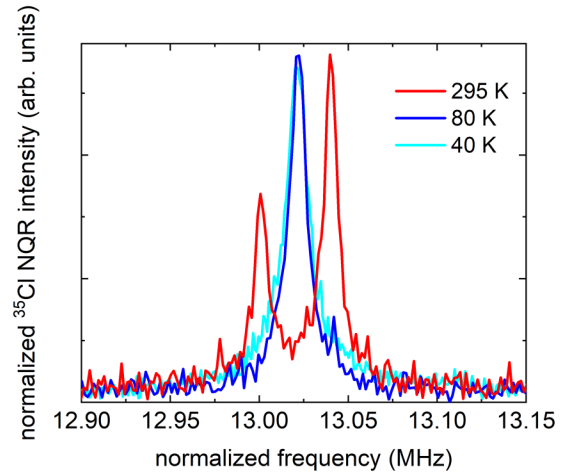


FIG. 9. ^{35}Cl NQR data of the CrCl_3 bulk single crystal measured at 295 K, at 80 K, and at 40 K. The spectra were shifted with respect to each other to illustrate the similarities and differences of the spectra taken at temperatures above and below the structural phase transition.

IV. RECONCILING THE NMR AND NQR DATA TO UNDERSTAND THE DIFFERENCES IN BULK SINGLE AND NANO CrCl_3 crystals

A. Low-temperature properties

The well-resolved ^{53}Cr three-peak-spectrum with spacing of about 0.22 MHz seen at lowest temperature $1.4 \text{ K} \leq T \leq 5 \text{ K}$ for the bulk single crystal corresponds to the majority of the Cr nuclei within the rhombohedral-type structure. The splitting into three individual, sharp lines with a frequency spacing of about 0.22 MHz (compare Sec. III D) originates in quadrupolar interaction. This value is consistent with the simulation yielding ν_c to be 0.22 ± 0.001 MHz (compare Sec. III E). With increasing temperature $5 \text{ K} \leq T < 7.5 \text{ K}$, the lines broaden. At higher temperature $7.5 \text{ K} < T \leq 10 \text{ K}$, these lines merge to an asymmetric one; the increasing line width results from increasing magnetic fluctuations and a broader distribution of local fields as the temperature approaches the magnetic ordering temperature (13 K; see Sec. III A).

The low temperature data for the nanocrystal show at least two quadrupole-split spectra plus a merged asymmetric broad line. The presence of more than one quadrupole-split spectrum indicates that at least two local and clearly discernible Cr environments exist in the nanocrystal. Those are, as minority contribution, also found in the high-frequency region of the bulk crystal spectra. Hence, the same local environments giving rise to the main contribution of the nanocrystal spectrum must be present as a minority fraction in the bulk crystal, too.

The surface to bulk ratio of the nanocrystal is not the source for the double features of the low-temperature NMR resonances as their approximate 1:1 spectral weight (54:46) is inconsistent with this scenario. This is a rather interesting result, and makes the discussed AlCl_3 -type surface reconstruction unlikely as the source of the suppressed structural transition in both exfoliated CrCl_3 and CrI_3 [34].

As second leading scenario to explain the absence of the structure transition in exfoliated CrCl_3 and CrI_3 is a

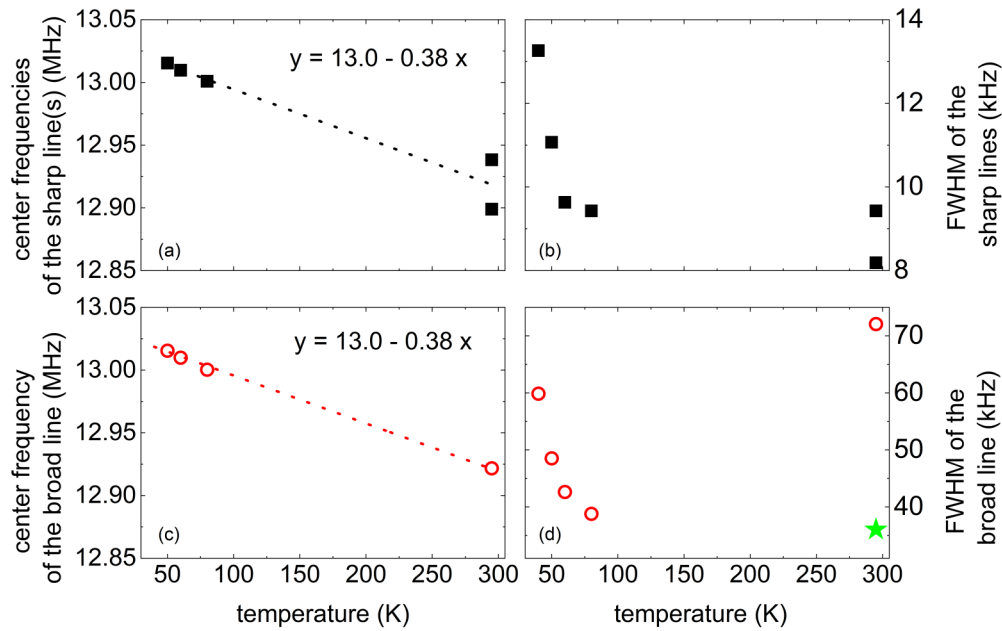


FIG. 10. Center frequency and FWHM from Gaussian fitting of the ^{35}Cl NQR data of the CrCl_3 bulk single crystal measured at different temperature. Black symbols represent the sharp lines, red dots symbolize the broad lines. The green star represents the hypothetical FWHM, assuming two broad lines for the 295 K data.

preservation of the high-temperature phase due to mechanical stress and the formation of stacking faults [34]. Typically, thin films relax upon reaching a certain thickness as the influence of the substrate decreases with increasing distance, thereby minimizing stress and strain. Such relaxation processes involve the formation of stacking faults. The majority of the nanocrystal flakes were determined to have a thickness above 2000 nm [4] and we can safely assume the largest part of the nanocrystal to be relaxed via formation of stacking faults. In addition, also the structural transition, as a first-order process, may lead to twinning. Those “defects” may account for a certain frequency shift and line broadening and even for line splitting, as strained thin films of Co with a thickness of 1.5 nm show a frequency shift of 2 MHz, corresponding to a strain of roughly 2% stemming from the lattice mismatch between Co and Cu [35].

B. Properties in the paramagnetic regime

The center frequencies for the sharp line (Cl nuclei in the rhombohedral structure) show a linear evolution for the low-temperature regime [Fig. 10(a)]. At 295 K, we see two sharp lines, as expected, associated with the two Cl positions in the high-temperature phase. Their center frequencies can be matched to the linear trend upon averaging. In case of the broad lines, we see a linear temperature evolution which closely resembles that for the sharp lines, therefore their origin is likely linked.

Similar to the frequencies, the FWHM of both the sharp and broad lines show a monotonous, nonlinear increase with decreasing temperature albeit inherently with different absolute values as for the frequencies. In analogy, the average of the FWHM for the two sharp lines at 295 K is consistent with the overall trend [Fig. 10(b)]. The FWHM of the broad

line at 295 K needs a division by two to follow the overall temperature evolution [green star in Fig. 10(d)].

Hence, the FWHMs and the center frequencies are rescaled by simple arithmetic to yield consistent trends. This suggests that the origin of all resonances is connected to a common source. In a hand-waving model, the broad line implemented in the fit at all temperatures may be interpreted to arise from a broad distribution of different local environments leading to a continuum of overlapping resonances. In this picture, the broad line at 295 K represents contributions from the low-temperature phase far above the transition temperature sensed by ^{35}Cl at two different sites, and the broad lines below actually represent two overlapping resonances on both sides of the distinct main line, signaling a fraction of the high-temperature phase far below the transition.

C. Structure of CrCl_3 above and below the transition

A coexistence of phases seen by ^{35}Cl NQR is consistent with the results from ^{53}Cr NMR at low temperature and is easily rationalized by the following arguments: Both structural modifications may be visualized as close-packed layer structures in which “honeycomb” sheets of chromium ions are separated by two layers of close-packed chlorine ions. In the high-temperature monoclinic structure, the chlorine atoms are almost face-centered cubic close-packed, while the low-temperature rhombohedral configuration is described by nearly hexagonal close-packed arrangement of chlorine. Hence, CrCl_3 exists in several variations which differ only in the packing arrangement of adjacent “honeycomb sandwiches” along the crystallographic c axis (compare Fig. 1). Accordingly, the mechanism of the structural transition is a simple translation of each sandwich along one direction [6,7,22,33]. This small difference between the structure types suggests a low energy barrier for translation, leading to

several stacking variations which differ only in the packing arrangement of adjacent honeycomb sandwiches along the crystallographic c axis. This low energy barrier may lead to a vast temperature region in which both phases coexist as only a small energy push may alter the local structure. This phenomenon is a special type of polymorphism (different crystal structures for the same chemical composition [34]) referred to as polytypism, which narrows the coexisting phases down to close-packed and layered materials with stacking variants [34].

Resuming along this line of arguments implies the following: (i) The sequence of phases is rather unusual as the high-temperature monoclinic phase has lower symmetry than the low-temperature rhombohedral phase. (ii) Interlayer interactions drive the transition as the honeycomb sandwich layers are not altered [22]. (iii) The transition is of first order, therefore a certain hysteresis is expected [7] along with twinning and formation of stacking faults. (iv) Given the different ^{53}Cr NMR data of the bulk and the nanocrystal, the specific ratio of the two polytypes depends on the thermal and magnetic history of a sample [7,22,34]. Therefore, kinetic aspects may play an important role for the evolution of phase formation in CrCl_3 .

Several magnetocaloric materials such as $\text{Ce}(\text{Fe}_{0.96}\text{Ru}_{0.04})_2$ [36] and FeRh [37] also show polymorphism. Interestingly, growth of their low temperature AFM phase out of a supercooled FM phase is strongly retarded [36], analogous to a glasslike phase formation where the supercooled phase appears to be frozen-in. This phenomenon is called kinetic arrest [36].

To illustrate the peculiarity of a kinetically arrested phase transformation, one may compare a conventional metastable supercooled state which will undergo metastable to stable transformation on lowering of temperature [38]. A metastable state that is kinetically arrested will conserve frozen-in domains of the high T phase even at lowest temperature, leading to a nonergodic inhomogeneous state.

Such structural domains and their evolution throughout the phase transition upon temperature cycling have recently been reported for the sister compound CrI_3 [39]. The authors concluded that the evolution of structure domains is kinetically driven.

For the present case of comparing a CrCl_3 bulk single crystal and a nanocrystal, the concept of a kinetic arrest of the phase transition where both phases form structural domains and both coexist at all temperatures, *viz.*, are frozen-in, consistently reconciles our zero-field ^{53}Cr NMR and ^{35}Cl NQR data. Moreover, the critical exponent β , derived by fitting the ^{53}Cr NMR data, may also hint at the formation of structural domains, thereby affecting the interlayer magnetic exchange.

Similar to our results, the early work by Narath also reported on the evolution of several resonance lines that dominate the NQR spectrum at a specific temperature range [6] whereas the temperature at which each line increases, decreases, or even vanishes is strongly sample dependent and not strictly determined by the structural transition temperature seen by diffraction [6,7].

Our interpretation is also consistent with the discrepancy between the structural model and the diffraction data devel-

oped during the monoclinic to rhombohedral phase transition as reported by McGuire *et al.* [7], with the strain-tunable magnetic anisotropy in monolayers of Cr(III) halides [9] and with different interlayer ferromagnetic ground states in bulk compared to native exfoliated thin films CrI_3 [15]. Therefore, the picture of a kinetically arrested phase transition with frozen-in structural domains whose size and/or number depend on the defect landscape suggests the macroscopic magnetic properties are even more complex than anticipated.

V. SUMMARY

We applied zero-field ^{53}Cr NMR and ^{35}Cl NQR spectroscopy to compare the properties of the van der Waals material CrCl_3 in two types of samples, namely, as bulk single crystal and as nanocrystals. An important finding is that the change from a monoclinic to rhombohedral structure is smeared out over a broad temperature range due to the low energy barrier between the high- and low-temperature phases. We also find indications for a kinetically arrested phase transformation. This arrest hinders the complete phase transition and, hence, the high-temperature phase is present at temperatures far below the expected transition temperature and vice versa. The nanocrystal is rather likely to be stressed or strained and relaxes by formation of stacking faults, leading to a pronounced kinetic arrest.

The different number of defects and stacking faults leads to further consequences for the magnetic properties. By fitting the evolution of the center of gravity of each zero-field NMR spectrum, we yield the critical exponent β , which is significantly different for both sample types. In analogy to a previous work on the van der Waals material $\text{Mn}(\text{Bi}_{1-x}\text{Sb}_x)_4\text{Te}_7$, a high number of defects as in the nanocrystal may give rise to additional interlayer magnetic exchange paths either directly as for the Mn antisites in $\text{Mn}(\text{Bi}_{1-x}\text{Sb}_x)_4\text{Te}_7$ or indirectly by causing the kinetically arrested phase transformation and, thereby, to coexistence of both structure types that, in turn, alter magnetic exchange.

This finding may, in part, explain the different magnetic properties found in different CrCl_3 samples since the presence of stress or defects may prevent a complete structural phase transformation with consequences for the magnetic properties that may even be more complex than anticipated.

ACKNOWLEDGMENTS

Financial support is acknowledged from the Deutsche Forschungsgemeinschaft (DFG) through Grants No. WU595/3-3, No. WU595/14-1, and No. HA5133/11-1, via Sonderforschungsbereich SFB 1143 (Project ID No. 247310070) and by Würzburg-Dresden Cluster of Excellence on Complexity and Topology in Quantum Matter – ct.qmat (EXC 2147, project-id 390858490). We thank R. Morrow, L. T. Corredor-Bohorquez, C. G. F. Blum, and A. Maljuk for discussions, S. Gaß for highly appreciated help with the magnetometry data, and H. M. Haghighi (all IFW) for support with magnetometry measurements.

- [1] A. Geim and K. Novoselov, *Nat. Mater.* **6**, 183 (2007).
- [2] A. Geim and I. Grigorieva, *Nature (London)* **499**, 419 (2013).
- [3] C. Gong, L. Li, Z. Li, H. Ji, A. Stern, Y. Xia, T. Cao, W. Bao, C. Wang, Y. Wang *et al.*, *Nature (London)* **546**, 265 (2017).
- [4] M. Grönke, B. Buschbeck, P. Schmidt, M. Valldor, S. Oswald, Q. Hao, A. Lubk, D. Wolf, U. Steiner, B. Büchner *et al.*, *Adv. Mater. Inter.* **6**, 1901410 (2019).
- [5] K. S. Burch, D. Mandrus, and J.-G. Park, *Nature (London)* **563**, 47 (2018).
- [6] B. Morosin and A. Narath, *J. Chem. Phys.* **40**, 1958 (1964).
- [7] M. A. McGuire, H. Dixit, V. R. Cooper, and B. C. Sales, *Chem. Mater.* **27**, 612 (2015).
- [8] B. Huang, G. Clark, E. Navarro-Moratalla, D. R. Klein, R. Cheng, K. L. Seyler, D. Zhong, E. Schmidgall, M. A. McGuire, D. H. Cobden *et al.*, *Nature (London)* **546**, 270 (2017).
- [9] L. Webster and J.-A. Yan, *Phys. Rev. B* **98**, 144411 (2018).
- [10] W. N. Hansen, *J. Appl. Phys.* **30**, S304 (1959).
- [11] D. MacNeill, J. T. Hou, D. R. Klein, P. Zhang, P. Jarillo-Herrero, and L. Liu, *Phys. Rev. Lett.* **123**, 047204 (2019).
- [12] I. Tsubokawa, *J. Phys. Soc. Jpn.* **15**, 1664 (1960).
- [13] W. N. Hansen and M. Griffel, *J. Chem. Phys.* **28**, 902 (1958).
- [14] J. Cable, M. Wilkinson, and E. Wollan, *J. Phys. Chem. Solids* **19**, 29 (1961).
- [15] T. Li, S. Jiang, N. Sivadas, Z. Wang, Y. Xu, D. Weber, J. E. Goldberger, K. Watanabe, T. Taniguchi, C. J. Fennie *et al.*, *Nat. Mater.* **18**, 1303 (2019).
- [16] Z.-P. Cheng, B.-G. He, H. Li, and W.-B. Zhang, *J. Phys.: Condens. Matter* **33**, 355401 (2021).
- [17] M. Roslova, J. Hunger, G. Bastien, D. Pohl, H. M. Haghghi, A. U. B. Wolter, A. Isaeva, U. Schwarz, B. Rellinghaus, K. Nielsch *et al.*, *Inorg. Chem.* **58**, 6659 (2019).
- [18] M. Newville, R. Otten, A. Nelson, A. Ingargiola, T. Stensitzki, D. Allan, A. Fox, F. Carter, Michał, R. Osborn *et al.*, *lmfit/lmfit-py*: 1.0.3 (2021), <https://doi.org/10.5281/zenodo.5570790>.
- [19] R. K. Harris, E. D. Becker, S. M. C. de Menezes, R. Goodfellow, and P. Granger, *Pure Appl. Chem.* **73**, 1795 (2001).
- [20] B. Herreros, A. W. Metz, and G. S. Harbison, *Solid State Nucl. Magn. Reson.* **16**, 141 (2000).
- [21] B. Kuhlow, *Phys. Status Solidi A* **72**, 161 (1982).
- [22] M. A. McGuire, G. Clark, S. KC, W. M. Chance, G. E. Jellison, Jr., V. R. Cooper, X. Xu, and B. C. Sales, *Phys. Rev. Mater.* **1**, 014001 (2017).
- [23] M. Majumder, M. Schmidt, H. Rosner, A. A. Tsirlin, H. Yasuoka, and M. Baenitz, *Phys. Rev. B* **91**, 180401(R) (2015).
- [24] Y. Kubota, H. Tanaka, T. Ono, Y. Narumi, and K. Kindo, *Phys. Rev. B* **91**, 094422 (2015).
- [25] S. T. Bramwell and P. C. W. Holdsworth, *J. Phys.: Condens. Matter* **5**, L53 (1993).
- [26] K. Krämer, H. Güdel, P. Fischer, F. Fauth, M. Fernandez-Diaz, and T. Hauss, *Eur. Phys. J. B* **18**, 39 (2000).
- [27] M. F. Collins, *Magnetic Critical Scattering* (Oxford University Press, New York, 1989).
- [28] M. E. Fisher, *Rep. Prog. Phys.* **30**, 615 (1967).
- [29] T. Qian, E. Emmanouilidou, C. Hu, J. C. Green, I. I. Mazin, and N. Ni, *Nano Lett.* **22**, 5523 (2022).
- [30] A. Narath, *Phys. Rev.* **131**, 1929 (1963).
- [31] A. Narath and A. T. Fromhold, *Phys. Rev. Lett.* **17**, 354 (1966).
- [32] A. Narath, *Phys. Rev. Lett.* **7**, 410 (1961).
- [33] M. A. McGuire, *Crystals* **7**, 121 (2017).
- [34] H. Bergeron, D. Lebedev, and M. C. Hersam, *Chem. Rev.* **121**, 2713 (2021).
- [35] G. J. Strijkers, J. T. Kohlhepp, H. J. M. Swagten, and W. J. M. de Jonge, *Appl. Magn. Reson.* **19**, 461 (2000).
- [36] M. K. Chattopadhyay, S. B. Roy, and P. Chaddah, *Phys. Rev. B* **72**, 180401(R) (2005).
- [37] D. J. Keavney, Y. Choi, M. V. Holt, V. Uhler, D. Arena, E. E. Fullerton, P. J. Ryan, and J.-W. Kim, *Sci. Rep.* **8**, 1778 (2018).
- [38] K. Kumar, A. K. Pramanik, A. Banerjee, P. Chaddah, S. B. Roy, S. Park, C. L. Zhang, and S.-W. Cheong, *Phys. Rev. B* **73**, 184435 (2006).
- [39] P. Doležal, M. Kratochvílová, D. Hovančík, V. Holý, V. Sechovský, and J. Pospíšil, *Inorg. Chem.* **63**, 976 (2024).